

- of purification. *J. Math. Phys.* **43**, 4286–4298 (2002).
- Schumacher, B. & Nielsen, M. A. Quantum data processing and error correction. *Phys. Rev. A* **54**, 2629–2635 (1996).
- Shor, P. The quantum channel capacity and coherent information. *MSR Workshop on Quantum Computation* (Berkeley, 2002); lecture notes available at (<http://www.msri.org/publications/hy/msr/2002/quantumcrypto/shor/>).
- Lloyd, S. The capacity of the noisy quantum channel. *Phys. Rev. A* **55**, 1613–1622 (1997).
- Dewetak, I. The private classical capacity and quantum capacity of a quantum channel. *IEEE Trans. Inf. Theory* **51**(1), 44–55 (2005).
- Yard, J., Dewetak, I. & Hayden, P. Capacity theorems for quantum multiple access channels—Part I: classical-quantum and quantum-quantum capacity regions (2005). Preprint at (<http://arXiv.org/quant-ph/0501045>) (2005).
- D'Vincenzo, D. P., et al. in *Proc. 1st NASA Int. Conf. on Quantum Computing and Quantum Communication* (ed. Williams, C. F.) LNCS 1509 247–257 (Springer, London, 1999).
- Smolin, J. A., Vershynov, F. & Winter, A. Entanglement of assistance and multipartite state distillation. Preprint at (<http://arXiv.org/quant-ph/0505038>) (2005).

- Li, E. H. & Ruskai, M. B. Proof of the strong subadditivity of quantum mechanical entropy with an appendix by B. Simon. *J. Math. Phys.* **14**, 1938–1941 (1973).
- Dewetak, I. & Winter, A. Relating quantum privacy and quantum coherence: an operational approach. *Phys. Rev. Lett.* **93**, 080501 (2004).

**Acknowledgements** This work was done at the Isaac Newton Institute (Cambridge) in August–December 2004 and we are grateful for the institute's hospitality. We thank W. Umrh for comments on an earlier draft of this paper. We acknowledge the support of EC grants RESQ, QUPRODIS and PROSECCO. M.H. was additionally supported by the Polish Ministry of Scientific Research and Information Technology, I.O. by the Cambridge-MIT Institute and Newton Trust, and A.W. by EPSRC's 'IRC QIP'.

**Author Information** Reprints and permissions information is available at <http://nature.com/reprintsandpermissions>. The authors declare no competing financial interests. Correspondence and requests for materials should be addressed to I.O. ([j.soppenheim@damtp.cam.ac.uk](mailto:j.soppenheim@damtp.cam.ac.uk)).

## Measurement of the conductance of single conjugated molecules

Tali Dadoosh<sup>1,2,3</sup>, Yoav Gordin<sup>1,2</sup>, Roman Krahne<sup>1,3</sup>, Ilya Khivrich<sup>1</sup>, Diana Mahalu<sup>1</sup>, Veronica Frydman<sup>3</sup>, Joseph Sperling<sup>2</sup>, Amir Yacoby<sup>1</sup> & Israel Bar-Joseph<sup>1</sup>

Electrical conduction through molecules depends critically on the delocalization of the molecular electronic orbitals and their connection to the metallic contacts. Thiolated (–SH) conjugated organic molecules are therefore considered good candidates for molecular conductors<sup>1,2</sup>; in such molecules, the orbitals are delocalized throughout the molecular backbone, with substantial weight on the sulphur–metal bonds<sup>3,4</sup>. However, their relatively small size, typically ~1 nm, calls for innovative approaches to realize a functioning single-molecule device<sup>5–11</sup>. Here we report an approach for contacting a single molecule, and use it to study the effect of localizing groups within a conjugated molecule on the electrical conduction. Our method is based on synthesizing a dimer structure, consisting of two colloidal gold particles connected by a thiolated short organic molecule<sup>12,13</sup>, and electrostatically trapping it between two metal electrodes. We study the electrical conduction through three short organic molecules: 4,4'-biphenyldithiol (BPD), a fully conjugated molecule; bis-(4-mercaptophenyl)-ether (BPE)<sup>14</sup>, in which the conjugation is broken at the centre by an oxygen atom; and 1,4-benzenedimethanethiol (BDMT), in which the conjugation is broken near the contacts by a methylene group. We find that the oxygen in BPE and the methylene groups in BDMT both suppress the electrical conduction relative to that in BPD.

Various methods have been suggested and realized to form nanometre-sized gaps, including electron beam lithography with shadow mask evaporation<sup>15</sup>, mechanical break junctions<sup>16,17</sup>, electromigration<sup>18</sup>, and side etched quantum wells<sup>19</sup>. Molecules are then deposited on the thin gap, and it is assumed that electrical conductivity is obtained when a single molecule bridges the gap and conducts current. Although impressive success in measuring the conductance of molecular junctions has been reported<sup>20–24</sup>, serious problems are evident. The most notable are the uncertainty about the number of conducting molecules in the junction, and the lack of information about the shape and structure of the metal contacts near the molecule. The dimer-based contacting scheme presented here provides several advantages. (1) Single-molecule devices can be fabricated with high certainty. (2) The contacts to the molecule are well defined and can be characterized separately. (3) Our scheme avoids the need for fabricating nanometre-sized gaps. (4) It also allows measurements of the temperature dependence of the molecular junction conductance over periods of hours and even days, regaining the original spectra after thermal cycling.

The dimer synthesis is performed by mixing a solution of thiolated molecules, whose structure is depicted in Fig. 1a, with a gold colloid, keeping their respective ratio below 1:10. The colloids were stabilized using the conventional citrate method<sup>25</sup>. In making the bridged dimers, the thiols on the bridging molecule displace citrate

anions to form stable Au–S bonds<sup>26</sup> (Fig. 1b, c). If more than one molecule binds to a certain colloidal particle, trimers (Fig. 1d), tetramers (Fig. 1e) and higher oligomers can be formed. To ensure that most of the dimeric colloidal particles are bridged by a single thiolated molecule, the concentration of the latter ( $C_m$ ) in the reaction mixture should be much smaller than the concentration of the monomeric colloidal particles ( $C_p$ ). In that case, when the reaction is completed, the ratio  $R$  of dimers to single unbound colloidal particles is expected to follow the relation  $R \approx C_m/(C_p - 2C_m)$ . We measured  $R$  for different input concentrations of thiolated molecules, keeping  $C_p$  fixed, and found that the above relation holds for  $C_m/C_p$  ratios that are lower than 1:10.

The dimeric colloidal particles are separated from monomeric particles and higher oligomers on the basis of their relative mass, by centrifugation through glycerol or sucrose density gradients. Each structure propagates as a different band across the centrifuged tube, and is easily distinguished because of its reddish colour. Figure 1f shows a transmission electron microscope (TEM) image at higher magnification of a dimer (made of two 10-nm colloidal gold particles connected by BDMT) that was synthesized in this manner. The gap between the two particles is readily seen, and its size is in good agreement with the size of the BDMT molecule, which is

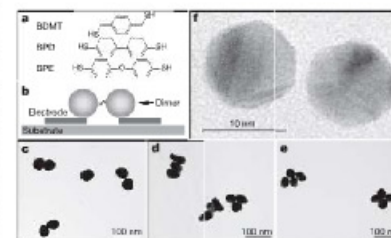


**Figure 1 | The molecules and colloidal structures under study. a**, The structures of the three molecules: 1,4-benzenedimethanethiol (BDMT), 4,4'-biphenyldithiol (BPD) and bis-(4-mercaptophenyl)-ether (BPE). **b**, The dimer contacting scheme. **c–e**, TEM images of BDMT dimer, trimer and tetramer structures made of 50-nm colloidal gold particles. **f**, TEM image of a BDMT dimer made of 10-nm colloidal gold particles. The ~1 nm separation between the two particles corresponds approximately to the BDMT length (0.9 nm).

<sup>1</sup>Department of Condensed Matter Physics, <sup>2</sup>Department of Organic Chemistry, <sup>3</sup>Chemical Research Support, Weizmann Institute of Science, 76100 Rehovot, Israel.

<sup>4</sup>Present address: National Nanotechnology Labs of INFN, Lecce 73100, Italy.

<sup>5</sup>These authors contributed equally to this work.

approximately 0.9 nm. To further establish the presence of a molecule in the dimer, we conducted Raman scattering measurements on dimers made from colloidal silver particles<sup>20</sup>. A clear Raman spectrum was detected from a single dimer, with the characteristic temporal blinking of a single molecule.

We position the dimer between two electrodes using the method of electrostatic trapping<sup>21,22</sup>. The gold electrodes are defined on a silicon substrate with a thin (25–100 nm) oxide layer using electron beam lithography. In most of our studies we use dimers of 30-nm-diameter colloidal gold particles. Hence, the electrodes are made with 40–50 nm separation, which is below the dimer size and larger than the diameter of a single particle. The processed structures are first cleaned<sup>23</sup> and then inserted in a probe station where the electrostatic trapping is performed.

The success rate of the electrostatic trapping is relatively high, and reaches ~50% when the impedance of the dimer solution is high enough, such that the dipole–dipole interaction between the electrodes and the colloids is not screened. An analysis of the trapping events reveals that in 55% of the cases the gap is bridged by one colloidal particle only. In 45% of the cases we get a dimer between the two electrodes (Fig. 2a). In 35% the conductivity is too low to determine the conductance features. We find in scanning electron microscopy (SEM) imaging that the brightness of the colloidal gold particles of these dimers is low, probably due to poor conductivity between one of the particles and the electrode<sup>24</sup>. In 10% of the trapping events we obtain high conductivity dimers. These are the samples that we refer to here: 11 BPD, 13 BPE and 15 BDMT devices.

Trapping single colloidal particles between closely spaced electrodes (25–30 nm) allows us to study the current–voltage characteristics of the contacts. For the 30-nm colloidal gold particles, we find a Coulomb blockade staircase with a single electron charging energy of ~20–30 mV, and by applying a voltage to the substrate we can measure the diamond structure of the conductance (see Supplementary Fig. 1) characteristic of a single-electron transistor<sup>25</sup>. It is evident that a tunnel barrier with a typical resistance of ~10 M $\Omega$  is formed between the gold particles and the electrodes, probably due to the ligands that stabilize the colloids in the solution.

The measurements of electrical transport through the dimer structures are performed using an a.c. voltage with an amplitude of a few millivolts superimposed on a d.c. voltage, and the current as well as the differential conductance ( $dI/dV$ ) are measured

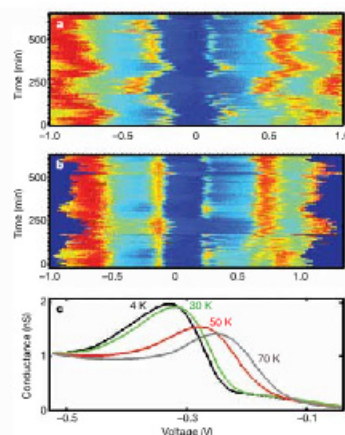


**Figure 3** | Temporal fluctuations and temperature dependence of the dimer conductance. **a**, A compilation of 130 measurements of the differential conductance spectrum of one BPD dimer, taken over a period of a few hours. The conductance values are represented by a colour scale, which ranges from blue (0 nS) to red (5 nS). **b**, The spectra of a shifted such that their peaks at  $-0.2$  V coincide, thus demonstrating the rigid shift nature of the temporal fluctuations. **c**, The evolution of the lowest voltage conductance peak of a BPD dimer with temperature. A decrease in height and broadening of the peak with increasing temperature is observed.

simultaneously. Figure 2b shows a comparison of the differential conductance of the three molecules at 4 K. These are representative curves from more than ten devices of each of the molecular species that were studied. The BPD dimers clearly show a series of conductance peaks. These peaks cannot be attributed to charging of the gold particles—their typical spacing is a few hundred millivolts, more than an order of magnitude larger than the charging energy of the particles. In fact, in some cases we could resolve the Coulomb blockade oscillations superimposed on the large conductance peaks (see Fig. 2c). The oscillation period is very similar to that observed in a single-particle measurement (see comparison in Supplementary Information). We note that the conductance through a single trapped colloidal particle is substantially higher than that of a dimer, typically by one to two orders of magnitude. Hence, the tunnel barriers between the metal electrodes and the gold particles act as small series resistances, carrying only a minute fraction of the applied voltage, while most of the voltage is dropped across the molecule.

The BPE and BDMT dimers show remarkably different behaviours. It is clearly seen that the conduction through the dimers formed from these molecules turns on at much higher voltages (typically larger than 0.5 V) and one cannot resolve any peak structure. The systematic difference between the three molecules further confirms that the measured differential conductance is of molecular origin. The apparent gap and exponential turn-on of the differential conductance in the case of the BPE and BDMT dimers suggest that adding localizing groups interferes with the conjugated aromatic system and suppresses the overall conductance through the molecule. This assertion is supported by comparing the BPE with the BPD molecule, where the addition of an oxygen atom between

the conjugated rings suppresses the conductance almost entirely below 1 V. A similar effect takes place in the BDMT dimers, where the methylene groups suppress the overlap of the molecular backbone orbitals with the contacts<sup>26</sup>.

Focusing on the peak structure of the BPD dimers, we find that while the main features of the conductance spectrum are highly reproducible, there are temporal fluctuations as well as variations between different devices. Figure 3a shows a compilation of 130 measurements of the conductance of one dimer taken over a period of a few hours. Strong temporal fluctuations in peak position, which could be as large as a few hundred millivolts, are evident. We find that the conductance spectrum shifts rigidly—that is, all peaks at positive and negative voltages move in the same direction by approximately the same value. This is demonstrated in Fig. 3b, where we shift all spectra such that their peaks at  $-0.2$  V coincide. It is seen that this operation causes all other peaks to be aligned as well. Such behaviour is typical of electrostatically gated Coulomb-blockaded systems with different input and exit capacitances<sup>27</sup>. Plotting the conductance in the  $V_{ds}$ – $V_g$  plane (where  $V_{ds}$  and  $V_g$  are the drain–source and gate voltages, respectively) produces a skewed diamond structure (see Supplementary Fig. 1b). It can be seen that under these conditions the conductance peaks at positive and negative drain–source bias indeed move rigidly on application of a gate voltage. As the gold particles are very effective in screening the effect of remote potentials, we conclude that charge movement in close vicinity to the molecule gives rise to the observed rigid shift of the spectrum. These temporal fluctuations can therefore be considered as evidence for gating of the molecule, which occurs randomly. We note that the temporal frequency of this random gating depends on the voltage sweep rate,  $dV/dt$ , and the voltage range of the measurement. It could be substantially minimized by working at low sweep rates and within a limited voltage range, such that stable and reproducible measurements can be conducted over hours.

The dimer structure allows us to conveniently perform measurements of the temperature dependence of the molecular junction conductance. We demonstrate this capability in Fig. 3c, which shows the behaviour of the lowest voltage peak ( $-0.3$  V in Fig. 3a) as the temperature is increased from 4 K to 100 K. It is evident that the peak broadens and decreases in height with increasing temperature, keeping the area approximately constant. The shift in peak position between the low- and high-temperature measurements is due

to gating, which occurred during this long measurement. The broadening of the peak can be accounted for by the change in thermal distribution of the electrons in the leads. This mechanism is expected to broaden the peak by  $-2k_B T$  (half-width at half-maximum), where  $k_B$  is the Boltzmann constant.

Comparing the conductance of nine BPD dimer-based devices shows that the variations between devices in the positions and relative strengths of the peaks cannot be explained only as a rigid shift. This is demonstrated in Fig. 4a, which compares the spectra of two BPD dimers. We can see that while the main features appear at approximately the same voltages, one cannot align the two spectra by a simple shift operation. We note also that there are differences in the value of the conductance between the various devices, which can be as large as an order of magnitude. To statistically quantify this variability, we construct a histogram of peak positions (Fig. 4b). This is done by converting each spectrum to a set of peaks, each represented by a block of unit height, a width which is the full-width at half-maximum, and is centred around its maximum. A rigid shift of each spectrum was allowed to accommodate the temporal fluctuations. It is seen that the peak structure survives the averaging over many molecules, indicating that the variability in peak position is smaller than the peak spacing. The peak positions determined from the histogram agree very well with measurements done on self-assembled monolayers of BPD<sup>28</sup>. However, such agreement is lacking when comparing the measured spectra with recent calculations of molecular conduction<sup>29</sup>. In particular, the measured turn-on voltage is significantly lower than theoretically predicted. Moreover, the predicted conductance is several orders of magnitude higher than observed.

## METHODS

Colloidal gold nanoparticles with a diameter of 30 nm were prepared using a method described by Graber *et al.*<sup>30</sup>, with slight modifications. Briefly, a solution of 'seed colloid' (2.6 nm) was prepared by adding 1.0 ml of 10 mg ml<sup>-1</sup> aqueous HAuCl<sub>4</sub>·3H<sub>2</sub>O to 100 ml of Milli-Q water while stirring. One min later, 1.0 ml of 10 mg ml<sup>-1</sup> aqueous trisodium citrate was added, followed, 1 min later, by 1.0 ml of freshly prepared 0.75 mg ml<sup>-1</sup> NaBH<sub>4</sub> in water, and the mixture was stirred for 5 min. Larger colloidal particles, 30 nm in diameter, were prepared by adding 0.2 ml of 10 mg ml<sup>-1</sup> trisodium citrate and 130  $\mu$ l of the Au 'seed colloid' solution to 50 ml of a boiling aqueous solution of HAuCl<sub>4</sub>·3H<sub>2</sub>O (0.1 mg ml<sup>-1</sup>) while stirring. Refluxing was continued for 10 min, or until a change to a reddish colour was observed. This procedure resulted in a citrate-stabilized colloid of gold particles well-dispersed in water; the particles had a narrow size distribution<sup>31</sup>, as confirmed by TEM. The concentration of colloidal gold particles was calculated on the basis of mean particle diameter measured by TEM and the weight of HAuCl<sub>4</sub> used in the reaction<sup>32</sup>.

The dimer preparation consisted of several stages. First, the colloidal gold solution was concentrated. This was achieved by centrifuging the solution at  $9.7 \times 10^3$  g for 5 min and discarding the supernatant. The precipitate was resuspended in 2.5 ml of 1 mM NaOH and centrifuged again as above, leaving about 0.4 ml of concentrated solution. The spacer diethanol molecule was dissolved in 0.1 M NaOH and diluted with 1 mM NaOH to the desired concentration. This solution was mixed with an equal volume of the concentrated colloidal gold solution containing  $>10$ -fold molar excess of colloidal particles and incubated for 24 h at 4 °C. The mixture (0.5 ml) was loaded on a 10–75% glycerol gradient in water and centrifuged at  $1 \times 10^5$  g for 10 min in a Beckman SW41 rotor. Fractions (0.5 ml) of the gradient were collected and characterized by TEM.

The electrodes are prepared on an electron beam defined pattern, and consist of 20 nm of Au on 10 nm of Ni that serves as an adhesion layer. The electrodes are cleaned in warm acetone and methanol for 5 min each, then placed in an ozone stripper for 8 min and finally stored in ethanol for 10 min (ref. 22).

Electrostatic trapping is performed in a probe station; a 0.35  $\mu$ l drop of the dimer solution (containing typically 45–55% dimers, 40–49% single particles and a few per cent of higher conjugates) is placed on the electrodes' surface. Next an a.c. voltage of 800 mV at 10 MHz is applied between the electrodes for 1 min. The sample is then cleaned in double distilled water, and blown dry in nitrogen. The devices are tested on the probe station, and the ones that show conductivity are bonded and measured at 4 K. After the measurement, the devices are imaged in an SEM to determine the type of colloidal structure that has been trapped.

679

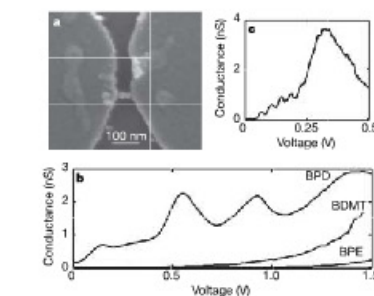


**Figure 2** | Image and low-temperature differential conductance spectra of dimers. **a**, SEM image of a dimer trapped between the two electrodes. **b**, The differential conductance as a function of voltage measured for BPD, BDMT and BPE dimers at 4.2 K. **c**, Coulomb blockade oscillations of the colloidal gold particle which are superimposed on the conduction peak of BPD measured at 4.2 K.

678

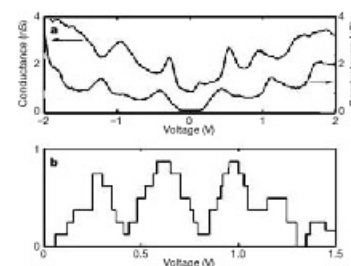


**Figure 4** | The reproducibility of the conductance spectra measurements of different BPD dimers. **a**, Comparison of the differential conductance spectrum of two different BPD devices (the upper curve has been shifted upwards for clarity). **b**, Histogram of the conductance peak positions collected from nine BPD devices. Each spectrum was converted to a set of peaks of unit height and a width which is the full-width at half-maximum. A rigid shift of the spectrum by up to 50 mV was allowed.



Received 20 January; accepted 7 June 2005

1. Nitzan, A. & Ratner, M. A. Electron transport in molecular wire junctions. *Science* **300**, 1384–1389 (2003).
2. Joachim, C., Gimzewski, J. K. & Aviram, A. Electronics using hybrid-molecule and mono-molecular devices. *Nature* **408**, 541–548 (2003).
3. Xue, Y. & Ratner, M. A. Microscopic study of electrical transport through individual molecules with metallic contacts. I. Band lineup, voltage drop, and high-field transport. *Phys. Rev. B* **68**, 115406–115418 (2003).
4. Remacle, F. & Levine, R. D. Electrical transmission of molecular bridges. *Chem. Phys. Lett.* **383**, 537–543 (2004).
5. Reed, M. A., Zhou, C., Muller, C. J., Burgin, T. P. & Taur, J. M. Conductance of a molecular junction. *Science* **278**, 252–254 (1997).
6. Reichert, J. et al. Driving current through single organic molecules. *Phys. Rev. Lett.* **88**, 176804 (2002).
7. Smith, R. H. et al. Measurement of the conductance of a hydrogen molecule. *Nature* **409**, 966–969 (2002).
8. Park, H., Lim, A. K. L., Alivisatos, A. P., Park, J. & McEuen, P. L. Fabrication of metallic electrodes with nanometer separation by electromigration. *Appl. Phys. Lett.* **75**, 301–303 (1999).
9. Park, J. et al. Coulomb blockade and the Kondo effect in single-atom transistors. *Nature* **407**, 722–725 (2002).
10. Liang, W., Shores, M. P., Bockrath, M., Lang, J. R. & Park, H. Kondo resonance in a single-molecule transistor. *Nature* **417**, 725–729 (2002).
11. Cui, X. D. et al. Reproducible measurement of single-molecule conductivity. *Science* **294**, 571–574 (2001).
12. Peng, X., Wilson, T. E., Alivisatos, A. P. & Schultz, P. G. Synthesis and isolation of a homodimer of cadmium selenide nanocrystals. *Angew. Chem. Int. Ed. Engl.* **36**, 145–147 (1997).
13. Broussseau, L. C. III, Novak, J. P., Marinakos, S. M. & Feldheim, D. L. Assembly of phenylacetylene-bridged gold nanocrystal dimers and trimers. *Adv. Mater.* **11**, 447–449 (1999).
14. Baroni, A. L. & Blank, D. R. Synthesis and properties of some aromatic polythiophenes. *Makromol. Chem.* **140**, 83–89 (1970).
15. Bearyadin, A., Dekker, C. & Schmidt, G. Electrostatic trapping of single conducting nanoparticles between nanoelectrodes. *Appl. Phys. Lett.* **71**, 1273–1275 (1997).
16. Krämer, R. et al. Fabrication of nanoscale gaps in integrated circuits. *Appl. Phys. Lett.* **81**, 730–732 (2002).
17. Park, H. et al. Nanomechanical oscillations in a single- $C_{60}$  transistor. *Nature* **407**, 57–60 (2000).
18. Grabar, K. C. et al. Two-dimensional arrays of colloidal gold particles: A flexible approach to macroscopic metal surfaces. *Langmuir* **12**, 2353–2361 (1996).
19. Wiesbeck, C. S., Merritt, M. V. & Whitesides, G. M. Molecular self-assembly of aliphatic thiols on gold colloids. *Langmuir* **12**, 3763–3772 (1996).
20. Xu, H. X., Bjerrild, E. J., Kall, M. & Björsson, L. Spectroscopy of single hemoglobin molecules by surface-enhanced Raman scattering. *Phys. Rev. Lett.* **83**, 4357–4360 (1999).
21. Amblar, I., Rawlett, A. M., Nagahara, L. A. & Tsui, R. K. An approach to transport measurements of electronic molecules. *Appl. Phys. Lett.* **80**, 2761–2763 (2002).
22. Ron, H., Mullis, S. & Rubinstein, I. Self-assembled monolayers on oxidized metals. 2. Gold surface oxidative pretreatment, monolayer properties, and deposition formation. *Langmuir* **14**, 1116–1121 (1998).
23. Hazari, M. et al. DNA-mediated self-assembly of carbon nanotube-based electronic devices. *Chem. Phys. Lett.* **391**, 389–392 (2004).
24. Grabert, H. & Devoret, M. H. (eds) *Single Charge Tunneling: Coulomb Blockade Phenomena in Nanostructures* (NATO ASI Ser. B, Vol. 294, Plenum, New York, 1992).
25. Xiao, X. Y., Xu, B. Q. & Tao, N. J. Measurement of single molecule conductances: Benzenedithiol and benzenedimethanethiol. *Nano Lett.* **4**, 267–271 (2004).
26. Lee, J. O. et al. Absence of strong gate effects in electrical measurements on phenylene-based conjugated molecules. *Nano Lett.* **3**, 115–117 (2003).
27. Zhu, T., Vasilev, K., Kreiter, M., Mitter, S. & Kneil, W. Surface modification of citrate-reduced colloidal gold nanoparticles with 2-mercaptoacetic acid. *Langmuir* **19**, 9518–9525 (2003).
28. Handley, D. A. in *Colloidal Gold—Principles, Methods, and Applications* (ed. Hayat, M. A.) 13–32 (Academic, New York, 1989).

Supplementary Information is linked to the online version of the paper at [www.nature.com/nature](http://www.nature.com/nature).

**Acknowledgements** This work was supported by the Minerva foundation. We thank R. Papovitz for assistance in obtaining the TEM image (Fig. 1f).

**Author Information** Reprints and permissions information is available at [www.nature.com/reprintsandpermissions](http://www.nature.com/reprintsandpermissions). The authors declare no competing financial interests. Correspondence and requests for materials should be addressed to J.B.-J. ([jbr@wisemil.wiwi-mann.ac.il](mailto:jbr@wisemil.wiwi-mann.ac.il)).

## Stability of the Larsen B ice shelf on the Antarctic Peninsula during the Holocene epoch

Eugene Domack<sup>1</sup>, Diana Duran<sup>1</sup>, Amy Leventer<sup>2</sup>, Scott Ishman<sup>3</sup>, Sarah Doane<sup>1</sup>, Scott McCallum<sup>3</sup>, David Amblas<sup>4</sup>, Jim Ring<sup>5</sup>, Robert Gilbert<sup>6</sup> & Michael Prentice<sup>7</sup>

The stability of the Antarctic ice shelves in a warming climate has long been discussed<sup>1</sup>, and the recent collapse of a significant part, over 12,500 km<sup>2</sup> in area, of the Larsen ice shelf off the Antarctic Peninsula<sup>2,3</sup> has led to a refocus toward the implications of ice shelf decay for the stability of Antarctica's grounded ice<sup>4–6</sup>. Some smaller Antarctic ice shelves have undergone periodic growth and decay over the past 11,000 yr (refs 7–11), but these ice shelves are at the climatic limit of ice shelf viability<sup>12</sup> and are therefore expected to respond rapidly to natural climate variability at century to millennial scales<sup>13</sup>. Here we use records of diatoms, detrital material and geochemical parameters from six marine sediment cores in the vicinity of the Larsen B ice shelf to demonstrate that the recent collapse of the Larsen B ice shelf is unprecedented during the Holocene. We infer from our oxygen isotope measurements in planktonic foraminifera that the Larsen B ice shelf has been thinning throughout the Holocene, and we suggest that the recent prolonged period of warming in the Antarctic Peninsula region<sup>14,15</sup>, in combination with the long-term thinning, has led to collapse of the ice shelf.

A marine geologic survey was conducted in the northwestern Weddell Sea (between 65°S and 66°S, and 59°W and 61°W) just before the dramatic collapse of a large portion of the Larsen ice shelf B (LIS-B; colloquially Larsen B ice shelf) in March 2002 (Fig. 1). Here we collected sediment cores, surface sediment grabs, bottom photographs and oceanographic profiles of temperature and salinity, and conducted a reconnaissance bathymetric survey (Figs 2 and 3). These data were collected in open water just east of the pre-collapse LIS-B front, but following a series of calving events resulting in shelf edge retreat before the 2002 collapse. Thus the LIS-B cores and an additional core<sup>16</sup> previously collected in the LIS-A region (core 23 in Fig. 1a) were located in a sub-ice shelf setting until 1995. Surface phytoplankton concentrations were estimated via ocean colour satellite imagery (Fig. 1c) and surface water sampling. The sediment cores recovered glacial and Holocene marine sedimentary sequences representing the transitions from glacial conditions to de-glacial (sub-ice shelf) conditions, and then to open marine conditions. Three stratigraphic intervals (units 3, 2 and 1) are recognized: a lower homogeneous diamictic (unit 3; glacial), a stratified to cross-stratified gravelly sand to granulated mud (unit 2; deglacial), and an upper laminated to homogeneous, slightly sandy mud (unit 1; sub-ice shelf) (Fig. 2b). Only the uppermost centimetre of unit 1, with higher bioturbation content, represents open marine conditions. These units are interpreted on the basis of a number of specific criteria in Antarctic glacial marine sequences<sup>17,18,19</sup>. The presence of glacial till (unit 3) is consistent with the glacially sculpted and streamlined sea floor documented from multibeam data (Fig. 1b)

and with a much expanded glacial regime on both sides of the Antarctic Peninsula (Fig. 1a; see Supplementary Information).

Termination of glacial cover upon the sea floor of both LIS-A and LIS-B is constrained by radiocarbon dates of 10,600 ± 55 years before present (yr BP) on calcareous foraminifera within the base of the sub-ice shelf facies, unit 1 in core KC-2 (Table 1), and palaeomagnetic intensity cross-dates of 10,700 ± 500 yr BP within LIS-A cores<sup>11</sup>. Radiocarbon ages on calcareous foraminifera and organic matter (Table 1) demonstrate that subsequent deposition beneath the LIS-B took place at progressively lower rates following deglaciation. In support of lithofacies interpretations is the twofold greater thickness for unit 1 within core KC-3, when compared to other cores (Fig. 2b). KC-3 is closest to the historical grounding line of the LIS-B around Jason Peninsula (Fig. 1b) and would be expected to have received glacial detritus at greater rates than sites more distal from the debris source (the grounding line).

All of the cores except KC-3 are characterized by concentrations of gravel at the sediment–water interface (Fig. 2a) marking the accumulation of coarse ice-rafted material. This is a result of a combination of coarse debris released when the ice shelf retreated to its penultimate position in 1998<sup>2</sup> and the rafting of poorly sorted stones under the distal reaches of the LIS-B, which was generally devoid of material except for englacial debris septa entrained at tributary junctures along the Antarctic Peninsula<sup>17</sup>. The inference that some of these stones resided exposed on the sea floor for some time is supported by the MnO<sub>2</sub> coatings of a few micrometres thickness over their surface, requiring at least 1.5–2.7 kyr to accumulate given observed rates of MnO<sub>2</sub> accretion in the Southern Ocean<sup>20</sup>. The surface of unit 1 is not a winnowed or lag surface but one of low sedimentation (Table 1) as <sup>10</sup>Be activities show near-surface excess beyond background levels (Fig. 3b), albeit associated with very low sediment accumulation rates (Table 1). Only a few of the large boulders recovered and observed in bottom photographs (Fig. 2b) show evidence of recent colonization by epifaunal organisms. All such organisms yield modern <sup>14</sup>C ages for biogenic calcite (Table 1, AA-49353 to AA-49358), attesting to the recent increase in advection of organic detritus to the sea floor in this area. Extremely low diatom abundance within all except the upper centimetre of unit 1 supports a sub-ice shelf origin for unit 1.

Quantitative downcore diatom data (Fig. 3a) indicate contrasting Holocene histories for LIS-A and LIS-B. It is notable that there is a much higher overall diatom concentration in KC23 (LIS-A) as contrasted to concentrations in LIS-B cores, which are several orders of magnitude lower, reinforcing the hypothesis that while the LIS-A region had no ice shelf for extended periods during the Holocene<sup>11</sup>, the LIS-B persisted through the Holocene until its recent collapse. A significant increase in absolute diatom concentration noted in some

<sup>1</sup>Department of Geosciences, Hamilton College, Clinton, New York 13323, USA. <sup>2</sup>Department of Geology, Colgate University, Hamilton, New York 13346, USA. <sup>3</sup>Department of Geology, Southern Illinois University, Carbondale, Illinois 62803, USA. <sup>4</sup>Department of Stratigraphy, Paleontology, and Marine Geosciences, University of Barcelona, 08028 Barcelona, Spain. <sup>5</sup>Physics Department, Hamilton College, Clinton, New York 13323, USA. <sup>6</sup>Department of Geography, Queen's University, Kingston, Ontario ON K7L 3N6, Canada. <sup>7</sup>Department of Earth Science, University of New Hampshire, Durham, New Hampshire 03824, USA.